AIAA-92-3738

Numerical Simulation of MPD Thruster Flows with Anomalous Transport

Giuliano Caldo, Edgar Y. Choueiri, Arnold J. Kelly and Robert G. Jahn
Electric Propulsion and Plasma Dynamics Laboratory
Princeton University, Princeton, NJ 08544
USA

AIAA/SAE/ASME/ASEE
28th Joint Propulsion Conference and Exhibit
July 6-8, 1992 / Nashville, TN

Numerical Simulation of MPD Thruster Flows with Anomalous Transport*

G. Caldo† E.Y. Choueiri‡ A.J.Kelly§ and R.G. Jahn¶
Electric Propulsion and Plasma Dynamics Laboratory
Princeton University
Princeton, New Jersey 08544, USA

Abstract

A fully two-dimensional, two-fluid numerical code has been specifically developed to study anomalous transport effects in an argon self-field coaxial MPD thruster. This model introduces several refinements to our previous work[1]. A finite volumes technique similar to that of Jameson[2] is used for the solution of the conservation equations, while concurrently solving the electromagnetic equations via a modified Jacobi method. This permits a faster and more accurate determination of spatial maps for the various steady-state flow and field properties to be computed. Also, in this paper, we extend the calculations to a *range* of typical operating conditions. The main goal is to compare the spatial distribution of these properties and the power dissipation in the thruster for simulation runs with and without anomalous transport. Anomalous transport theory takes into account the interaction between plasma waves and charged particles due to microinstabilities. A conductivity law based on the non-linear saturation of the lower hybrid current-driven instability[3] is used for the calculations. Comparisons with experimental performance show that anomalous effects may help the accuracy of fluid simulation of MPD thruster flows. Runs with anomalous transport for a geometry similar to the Full-scale Princeton Benchmark thruster (FSBT) revealed that the resistivity, in specific regions of the discharge (especially near the anode), is significantly higher than that calculated from classical runs. Dissipation was also enhanced and the thrust efficiency was adversely impacted by the microturbulence dropping by 13% at $J^2/\dot{m} = 55$ kA^2 sec/g.

*This work is supported by the Air Force Office of Scientific Research under contract AFOSR-91-0162 and the National Aeronautics and Space Administration under contract NASA-954997.

†Graduate Student

‡Research Associate

§Senior Research Staff

¶Professor

Nomenclature

B	magnetic field strength
F	Thrust
E	electric field
J	total interelectrode current
j	current density
σ	electrical conductivity
ψ	electromagnetic stream function
k	Boltzmann's constant, heat transfer coefficient
m	mass
$\dot{m}$	mass flow rate
e	elementary charge
μ_o	permeability of free space
ϵ_o	permittivity of free space
n	number density
ρ	mass density
p	pressure
T	temperature
E_l	electron-ion energy exchange rate
v	plasma streaming velocity
Ω	electron Hall parameter
ν	collision frequency
r	radial coordinate
z	axial coordinate
t	time

Subscripts

e	electron
i	ion
n	neutral
h	heavy species
AN	anomalous
t	thermal
d	drift

Introduction

In the past twenty years, the flow modeling of MPD thrusters has evolved from rudimentary analytical attempts[4] to sophisticated two dimensional, two-fluid treatments[5, 1, 6]. The main goal of thruster modeling is to understand the dominant physical processes occurring in the thruster chamber and in the plume, in order to help drafting design criteria for improved prototypes. Plasma fluid flow models of the MPD thruster aim at predicting the following items:

- *Thrust.* The thrust of a coaxial self-field MPD thruster is usually well predicted by the Maecker law[7], ($F = bJ^2$), for sufficiently high values of $J^2/\dot{m}$ (or equivalently high specific impulse). Most fluid models to date can easily reproduce the Maecker law at high specific impulse due to the fact that the Lorentz term in the momentum equation dominates. At low specific impulse, however, the measured thrust of the MPD thruster is known to exceed the Maecker law and here the accuracy of a model can be tested against experimental data (as will be done in Section 3.1). The more interesting questions for fluid models are not related to the momentum side of the problem but rather to the energetics. It is, however, conceivable that fluid models can be used to investigate the problem of thrust enhancement due to electrothermal forces that may be at play under high pressure conditions. Moreover, the thrust (or momentum) problem is paramount for simulations of thrusters with applied magnetic field.

- *Voltage and Efficiency.* A crippling feature of self-field MPD thrusters is their low measured thrust efficiency, which has never been reported to be above 30% for argon. Most models to date have predicted efficiencies above 50%, especially for high power. A model by Niewood and Miller[5, 8] predicts relatively lower efficiency due to viscous dissipation for thrusters with long, narrow chambers; however, for thrusters with high width/length aspect ratio, as is the case of the Princeton Benchmark thruster, or for low mass flow rate devices, viscous dissipation cannot explain poor performance. A successful prediction of MPD thruster efficiency will have to take into account some dissipation mechanism which applies to all thruster geometries for high enough specific impulse.

- *Critical Regimes and Critical Regions.* MPD thruster operation is severely impaired by such effects as electrode and backplate erosion some of which occur at operation in critical regimes and at critical locales in the discharge. These effects limit the lifetime and the overall performance of the thruster. Fluid flow models can help in the investigation of the nature and dependencies of such critical regimes and "hot spots".

In the past five years much research has been done on dissipative microinstabilities which hold promise to shed light on the energy dissipation and low efficiency problems. Choueiri[3, 9] has identified plasma wave-particle interactions which have the effect of drastically reducing the conductivity and of raising particle heating in specific regions of the thruster. Furthermore, Choueiri[10] and Tilley[11, 12], have found direct experimental evidence of the predicted microinstabilities in high and low power MPD thrusters, respectively.

This paper integrates Choueiri's theoretical results into a two-fluid, two-dimensional axially symmetric simulation model, in order to study the bearing that anomalous transport has on local dissipation and on overall thrust efficiency. Several improvements have been made with respect to our initial study[1]. First of all, the numerical model has been modified for greater speed and accuracy in the solution of the differential equations. Furthermore, a non-ideal equation of state for the ions has been introduced (see section 1.2). The code has been run for various current levels, so that performance curves could be obtained and compared with experiments. Finally, the thruster dimensions have been modified in order to match as much as possible (while keeping the longitudinal cross-section rectangular) the Full Scale Benchmark Thruster (FSBT) configuration shown in Fig. (5). This change has turned out to greatly increase the electron Hall parameter near the electrodes and to therefore increase anomalous dissipation since the magnitude of the latter is controlled by the electron Hall parameter[3]. The effects of anomalous dissipation on the overall thruster performance are discussed by comparing the predicted performance with experiments (Section 3.1). In Section 3.3 we compare the predictions of codes with and without anomalous transport.

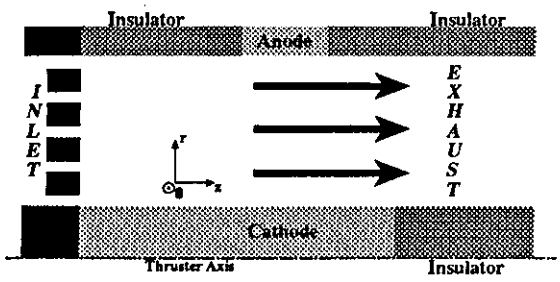

Figure 1: Simplified thruster geometry used for computation.

1 MPD Thruster Model

1.1 Geometry

A simple cylindrical geometry with constant cross-section is employed for this study. While a constant cross-section may somewhat mute the effects of anomalous transport it has the great benefit of simplicity and a smaller computational burden than more realistic geometries. These will be studied as part of subsequent work. The electrodes and insulators were taken to have dimensions similar to those of the Full-Scale Benchmark Thruster (FSBT). An in-scale cross-section of the chamber is schematically displayed in Fig. (1). The overall dimensions of the computational domain are 210 mm × 35 mm. A most important difference between the real and modeled geometries is the presence of upstream insulators in the latter. The simulation of the free-boundary exhaust jet would require the removal of these insulators. This will however jeopardize the simplicity afforded by the constant cross-section assumption and will consequently be postponed for our next study.

1.2 Assumptions

A two-fluid, axisymmetric, two-dimensional model has been developed to study the effect of anomalous dissipation on accelerator physics. Electron and heavy species energies, as well as electron and heavy species densities, are separately conserved. The flow is assumed to be nonviscous. Electron-electron and ion-ion heat conduction is included. It is also assumed that the electrons obey the ideal gas law, while the ions obey a non-ideal equation of state of the form

$$\frac{p_h}{\rho} = f(T_h). \tag{1}$$

The numerical derivation of this equation from accurate argon partition functions is discussed in reference[13]. A Hall term has been introduced in Ohm's law, and no applied magnetic field is assumed.

1.3 Boundary Conditions

At the inlet, the heavy species temperature is fixed to 10^4 K, the mass flow rate to 6 g/s, and the Mach number to 1. The electron temperature, furthermore, is taken to satisfy $\partial T_e/\partial z = 0$ at $z = 0$. The radial velocity is set to 0. The value of the total current J specifies the stream function boundary value: $\psi = 4\pi J/\mu_0$. The fluid velocity is determined from the Mach number and the heavy species temperature. The inlet density is taken to be uniform and such that $2\pi \int_r \rho v_r r dr = \dot{m}$. The ionization ratio is taken so as to make $\dot{n}_e = 0$, i.e., there is no net electron production at the inlet.

The heavy species temperature at the walls is again set to 10^4 K, and the electron normal derivative is zero. The radial velocity at the walls is also nil.

At the upstream insulators ψ is equal to the inlet value, while at the downstream insulator and at the outlet it is set to zero. At outflow, the axial derivatives of p_e, p_h, ρ, ρ_e, and v_z are set to zero.

1.4 Equations

1.4.1 Conservation Laws

The heavy species mass, electron mass, and total momentum conservation equations are expressed in the form

$$\frac{\partial \rho}{\partial t} + \frac{\partial}{\partial z}(\rho v_z) + \frac{\partial}{\partial r}(\rho v_r) = -\frac{\rho v_r}{r}, \tag{2}$$

$$\frac{\partial \rho_e}{\partial t} + \frac{\partial}{\partial z}(\rho_e v_z) + \frac{\partial}{\partial r}(\rho_e v_r) = -\frac{\rho_e v_r}{r} + m_e \dot{n}_e, \tag{3}$$

$$\frac{\partial}{\partial t}(\rho v_z) + \frac{\partial}{\partial z}(\rho {v_z}^2 + p) + \frac{\partial}{\partial r}(\rho v_z v_r) = -\frac{\rho v_r v_z}{r} + j_r B_\theta, \tag{4}$$

$$\frac{\partial}{\partial t}(\rho v_r) + \frac{\partial}{\partial z}(\rho v_z v_r) + \frac{\partial}{\partial r}(\rho {v_r}^2 + p) = -\frac{\rho {v_r}^2}{r} - j_z B_\theta, \tag{5}$$

where $\dot{n}_e$ is calculated using the Hinnov-Hirshberg theory of ionization-recombination[14].

The electron and heavy species energy conservation laws are expressed in terms of the respective pressures:

$$\frac{\partial}{\partial t}(\tfrac{3}{2} p_h) + \frac{\partial}{\partial z}(\tfrac{3}{2} p_h v_z) + \frac{\partial}{\partial r}(\tfrac{3}{2} p_h v_r) = -\frac{5 p_h v_r}{2r}$$

$$- p_h(\frac{\partial v_z}{\partial z} + \frac{\partial v_r}{\partial r}) + \frac{\partial}{\partial z}(k_h\frac{\partial T_h}{\partial z}) + \frac{\partial}{\partial r}(k_h\frac{\partial T_h}{\partial r}) + E_l + (Q_i)_{AN}, \quad (6)$$

$$\frac{\partial}{\partial t}(\tfrac{3}{2}p_e) + \frac{\partial}{\partial z}(\tfrac{3}{2}p_e v_{xe}) + \frac{\partial}{\partial r}(\tfrac{3}{2}p_e v_{re}) = -\frac{5p_e v_{re}}{2r} - p_e(\frac{\partial v_{ze}}{\partial z} + \frac{\partial v_{re}}{\partial r}) + \frac{\partial}{\partial z}(k_e\frac{\partial T_e}{\partial z}) + \frac{\partial}{\partial r}(k_e\frac{\partial T_e}{\partial r}) - E_l + \frac{{j_r}^2 + {j_z}^2}{\sigma_{eff}}, \quad (7)$$

where the ions are heated by the turbulent fluctuations at a rate $(Q_i)_{AN} = \frac{3}{2}(\nu_i^T)_{AN}T_h$. The anomalous heating rate $(Q_i)_{AN}$ and σ_{eff}, the effective conductivity are computed using Choueiri's anomalous transport models cast in polynomial form[3, 1].

In that work, a two-parameter, variable cross-term, least square fit was made to the calculated heating and momentum exchange rates in order to include them in the flow code. The resulting polynomial are quoted below

The interpolating polynomial for $(\nu_i^T)_{AN}/\nu_{ei}$ has an average accuracy of 15% and reads

$$\frac{(\nu_i^T)_{AN}}{\nu_{ei}} = 5.36\times10^{-5} + 1.29\times10^{-5}\ \Omega + 6.03\times10^{-6}\ \Omega^2 + 9.44\times10^{-8}\ \Omega^3 + \frac{T_h}{T_e}(-7.55\times10^{-7} - 5.41\times10^{-6}\ \Omega - 3.93\times10^{-6}\ \Omega^2). \quad (8)$$

The effective conductivity introducing the anomalous resistivity effect to the flow code has the form

$$\sigma_{eff} = \frac{e^2 n_e}{m_e(\nu_{ei} + (\nu_e^P)_{AN})}, \quad (9)$$

where $(\nu_e^P)_{AN}$ is the electron-wave momentum exchange frequency, which is again computed through an interpolating polynomial of average accuracy of 10%

$$\frac{(\nu_e^P)_{AN}}{\nu_{ei}} = 0.192 + 3.33\times10^{-2}\ \Omega + .212\Omega^2 - 8.27\times10^{-5}\ \Omega^3 + \frac{T_h}{T_e}(1.23\times10^{-3} - 1.58\times10^{-2}\ \Omega - 7.89\times10^{-3}\ \Omega^2). \quad (10)$$

Anomalous dissipation is onset when the ratio u_{de}/v_{ti} equals or surpasses 1.5 as was found in ref. [9] for the parameter-space covered by our simulations. At all the gridpoints where $u_{de}/v_{ti} < 1.5$ both, $(\nu_e^P)_{AN}$ and $(\nu_i^T)_{AN}$ are set to zero and all transport is assumed purely classical. Otherwise, the anomalous rates are computed from the above polynomials using the instantaneous macroscopic parameters and folded back into the flow equations at every time step thus insuring self-consistency. For a discussion of the calculation of $(Q_i)_{AN}$ and σ_{eff} from the solution to the dispersion relation, see ref. [3].

The heat transfer coefficients are those derived in Mitchner and Kruger[14]. The electron-ion energy exchange rate is

$$E_l = 3\frac{\rho_e}{m_h}\nu_{ei}k(T_e - T_h).$$

The total electron axial and radial speeds are defined as

$$v_{ze} = v_z - \frac{j_z}{en_e}, \qquad v_{re} = v_r - \frac{j_r}{en_e}. \quad (11)$$

1.4.2 Electromagnetic Equation

If we define $\psi \equiv B_\theta r$, we can write an equation for ψ derived from the generalized Ohm's law and Maxwell's equations[1]:

$$\frac{\partial^2\psi}{\partial z^2} + \frac{\partial^2\psi}{\partial r^2} + \gamma_1\frac{\partial\psi}{\partial z} + \gamma_2\frac{\partial\psi}{\partial r} + \gamma_3\psi = 0, \quad (12)$$

where

$$\gamma_1 = -\frac{1}{\sigma}\frac{\partial\sigma}{\partial r} - \frac{\psi\sigma}{r}\frac{\partial\frac{1}{en_e}}{\partial r} + \frac{2\sigma}{en_e r^2}\psi - \mu_0\sigma v_z,$$

$$\gamma_2 = -\frac{1}{\sigma}\frac{\partial\sigma}{\partial z} + \frac{\psi\sigma}{r}\frac{\partial\frac{1}{en_e}}{\partial z} - \frac{1}{r} - \mu_0\sigma v_z,$$

$$\gamma_3 = -\mu_0\sigma\psi(\frac{\partial v_z}{\partial z} + \frac{\partial v_r}{\partial r} - \frac{v_r}{r}).$$

2 Numerical Model

The flow field code uses a finite volumes discretization with artificial dissipation described by Jameson[2]. The time stepping is done via the explicit Euler Forward method, and convergence is accelerated using a multigrid iteration first proposed by Jameson and Jayram[15]. These methods yield a second order steady-state solution to the conservation equations.

The solution of the conservation equations through the finite volumes/Euler forward routine is alternated with the solution of the electromagnetic equation, until consistency among all the parameters is achieved.

The stream function equation 12 is solved with a second-order nonlinear explicit scheme developed at EPPDyL. After a central difference discretization is performed, equation 12 assumes the form

$$\zeta_1 \psi_{ij} + \zeta_2 = 0. \tag{13}$$

Here ψ_{ij} stands for the value of ψ at the i^{th} horizontal and j^{th} vertical discrete steps. The coefficients ζ_1 and ζ_2, then, are functions of the differential equation's coefficients and of $\psi_{i-1,j}$, $\psi_{i+1,j}$, $\psi_{i,j-1}$, $\psi_{i,j+1}$ Each iteration step we set

$$(\psi_{ij})^{(n+1)} = -\left(\frac{\zeta_2}{\zeta_1}\right)^{(n)}, \tag{14}$$

until $(\psi_{ij})^{(n+1)}/(\psi_{ij})^{(n)}$ is equal to 1. Using as initial guess the value of ψ computed at the previous MacCormack step, convergence is achieved in a number of steps ranging between 1 and 250.

These methods represent an improvement with respect to the MacCormack method used previously since it decreases running time by up to a factor of eight while reducing the steady-state residual. The model was coded in APL2 (taking full advantage of the inherent vectorizing capability of the language) and has been run on a variety of machines ranging from a Mac Quadra (1.2 Mflops) to an IBM ES/3090 600J Supercomputer where specialized APL2 compilers can allow convergence to be reached in less than 30 minutes of CPU time.

3 Results

This section will first discuss the performance curves obtained running at various current levels, with and without anomalous transport, and compare them to experimental data taken by Burton for a FSBT[16]. Two high current runs (18 kA), one with classical and one with anomalous dissipation, will then be compared, in order to asses in what areas of the thruster anomalous transport has the greatest impact. Furthermore, current distribution patterns will be compared with measured ones. The current density distribution for simulations with and without anomalous transport will also be shown, together with an experimental distribution obtained by Gilland[17].

Henceforth, the runs in which the conservation equations include anomalous transport coefficients will be denoted as "anomalous", whereas those not containing anomalous transport will be called "classical runs".

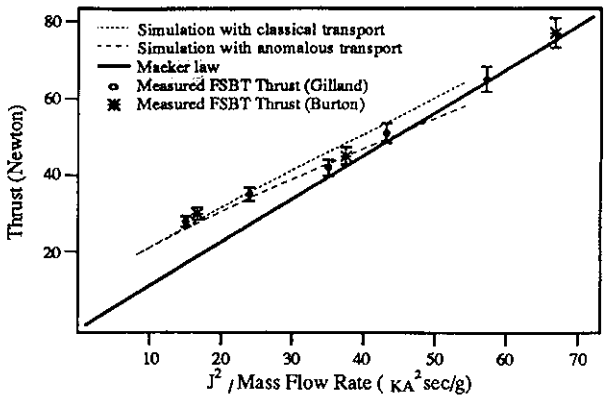

Figure 2: Calculated thrust from simulations with and without anomalous transport compared with measured FSBT thrust measured by Gilland[17] and Burton[16].

3.1 Discussion of Performance Curves

The code was run with a mass flow rate of 6 g/s and with currents ranging from 7 kA to 18 kA. The code diverged for higher currents. Runs were made both with and without anomalous transport dissipation terms present in the calculation. Plots of thrust, voltage and efficiency versus $J^2/\dot{m}$ are shown for these runs along with experimental data when appropriate.

As is evident from Fig. (2), thrust scales as the square of the current individually for the case with and without anomalous transport. Both classical and anomalous predictions compare very well with the measured Benchmark values, which in turn are very close to the theoretical Maecker thrust[7] for the higher range of specific impulse ($J^2/\dot{m} \geq 40$ kA^2 sec/g). At lower values of $J^2/\dot{m}$, the measured thrust data exceed the Maecker law prediction. The simulations, however, were able to account for that excess as can be seen from the figure. It is also important to note that the thrust from the anomalous run becomes appreciably lower as $J^2/\dot{m}$ increases. This may be attributed to the fact that for higher T_h (anomalous case), the gas pressure decreases less along the chamber, so that the $-\nabla p_h$ force term is reduced.

Figure (3) shows the calculated voltage drop across the plasma (from the anode to the cathode). The calculated voltages do not include electrode sheath falls and therefore cannot be easily compared to the measured terminal voltage of the thruster. The volt-

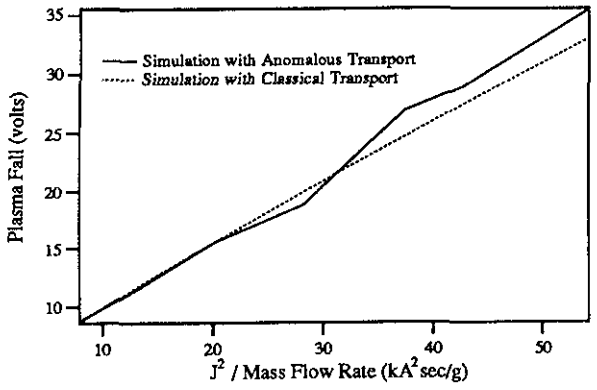

Figure 3: Plasma fall for simulations with and without anomalous transport. The calculated voltage does not include electrode sheath falls.

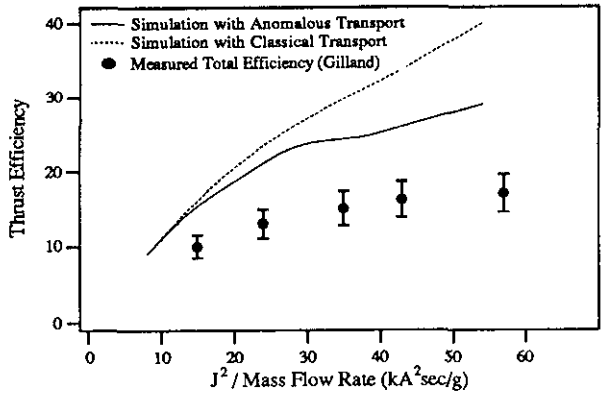

Figure 4: Thrust efficiency for simulations with and without anomalous transport compared with measured FSBT values.

age starts being consistently higher in the anomalous case only for the higher currents (above around 40 kA^2 sec/g).

The increase in the voltage and the decrease in thrust, due to anomalous transport, translate directly into a degradation in the thrust efficiency. To see the extent of this degradation, the thrust efficiency is calculated through the formula

$$\eta = \frac{F^2}{2\dot{m}JV}. \qquad (15)$$

In Fig. (4) the efficiency is plotted, again, versus $J^2/\dot{m}$. While for currents below 10 kA ($J^2/\dot{m} \leq 20\ kA^2$ sec/g) there is hardly any difference between the classical and the anomalous cases, for higher currents the efficiency is substantially lower with anomalous transport dropping by 13% at $J^2/\dot{m} = 55\ kA^2$ sec/g. Furthermore, efficiency from anomalous runs tends to reach a plateau around 25% for $J^2/\dot{m} \geq 30\ kA^2$ sec/g, while in the classical transport case it keeps increasing. The shape of the efficiency curve for the anomalous runs, then, is closer to the plateau shape of the experimental curve. Even the lower efficiencies predicted by the simulation with anomalous transport are higher than the experimentally measured values. This discrepancy is due to a large extent to the fact that this numerical simulation does not include the voltage drops from the electrode sheaths. If the experimental total voltage were reduced by the sheath voltage, the numerical and experimental curves would approach each other significantly. Gallimore[18], in fact, has shown that the anode fall voltage increases monotonically with $J^2/\dot{m}$, and reaches values as high as 40 volts around $J^2/\dot{m} = 50\ kA^2$ sec/g. Greater accuracy may be expected with the use of a more accurate geometric thruster configuration (with a varying cross-section) through the introduction of a transformation of coordinates in the model's equations. This will be the next step in our future studies. Furthermore, the extent to which viscous effects may help approaching the experimental values will also be explored in future investigations.

3.2 Current Distribution

Current distribution in a full-scale Princeton Benchmark Thruster for $J^2/\dot{m} = 30\ kA^2$ sec/g is shown in Fig. (5) as measured by Gilland[17]. Current distribution as predicted by the anomalous transport numerical simulation is also shown (Fig. (6)).

It can be noted from these two figures that, along the cathode, which is the region where the geometric configurations are most similar, the calculated current distribution is evenly spread as in the experiments, with attachment going all the way to the root. Furthermore, the current pattern *inside* the discharge chamber is well predicted both in shape (contour lines curvature and inclination) and magnitude. This is the case up to the 60% line downstream of which the calculated current does not "balloon" out as much as in the experiments undoubtedly because of the presence of the downstream insulators imposed on the modeled geometry. Particularly, the insulator downstream of the anode does not allow attachment to the anode front like in the experiments.

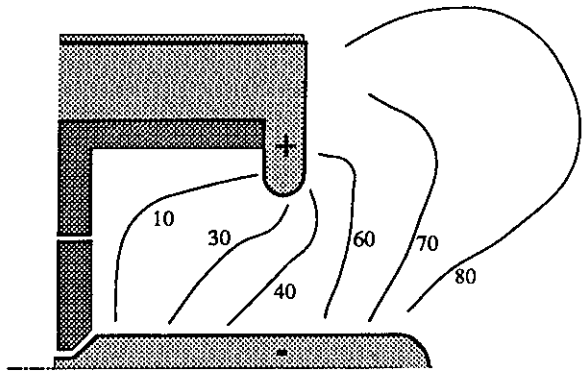

Figure 5: Current contour lines, in percentage of enclosed total current, as measured by Gilland[17]. ($J^2/\dot{m} = 30$ kA^2 sec/g).

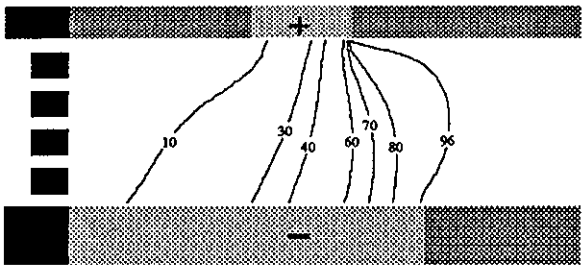

Figure 6: Current contour lines, in percentage of enclosed total current, as predicted by a flow model with anomalous transport. ($J^2/\dot{m} = 30$ kA^2 sec/g).

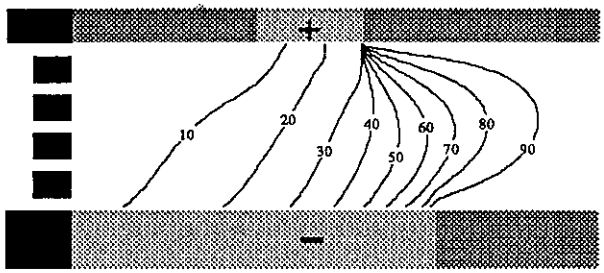

Figure 7: Enclosed current lines for the simulation with classical transport ($J = 18$ kA, $\dot{m} = 6$ g/s). The number along each line indicates what percentage of the total current is upstream of the line.

3.3 Comparison Between a Classical and an Anomalous Run for High Current

We will now present two runs, one with classical and one with anomalous transport, at a current level of 18 kA and a mass flow rate of 6 g/s, and discuss the most striking differences between the two. In particular, resistivity and plasma heating will be shown to be significantly enhanced by plasma microturbulence.

Of course, changing the conductivity as a result of anomalous effects may affect the current attachment on the electrodes. Figures (7) and (8) show the distribution of current for the classical and for the anomalous runs. Since the conductivity is higher in the plume, for the classical case the current is blown more downstream. Furthermore, there is greater attachment at the tip of the anode for the classical run, again because of the higher relative conductivity there as will become apparent from the resistivity plot shown further below.

As mentioned above, anomalous transport is possible only in regions where u_{de}/v_{ti} exceeds 1.5. Moreover, once anomalous transport effects are onset in a certain region, their magnitude increases monotonically with the electron Hall parameter as can be seen from Eqs. (8) and (10). Figure (9) shows a map of the electron Hall parameter, Ω_e, in locations at which anomalous transport arises (i.e. regions with $u_{de}/v_{ti} \geq 1.5$). For such high a current as 18 kA, and unlike the case investigated in our last study[1], anomalous transport can be expected to affect a substantial portion of the discharge. The plot in Fig. (9) directly allows the identification of critical regions of

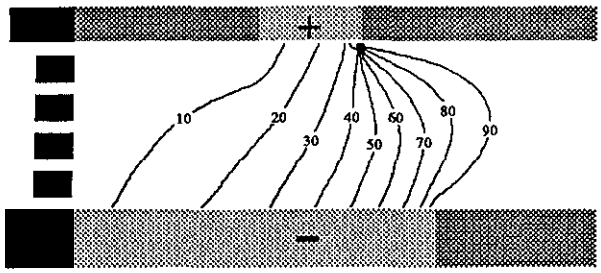

Figure 8: Enclosed current lines for the simulation with anomalous transport ($J = 18$ kA, $\dot{m} = 6$ g/s).

the discharge from the point of view of anomalous transport. It is evident that the cathode root and tip and the anode tip are most critical.

The criticality of these regions is further supported by the resistivity map of Fig. (10) where the ratio of "anomalous" to "classical" resistivities (i.e. using the resistivities calculated from the anomalous and classical runs) is shown. The pronounced anomalous resistivity enhancement in the immediate vicinity of the anode tip is very reminiscent of the enhanced resistivities inferred by Gallimore[18] from local measurements near the anode. This further substantiates our earlier speculations[9, 1, 3] that a substantial part of the infamous "anode drop" may be related to the turbulent effects induced by microinstabilities.

An appreciation of the extent and regional preference of anomalous plasma heating can be obtained by comparing the maps of Fig. (11) and Fig. (12). The two maps are of the ion temperature from the classical and anomalous runs respectively. It is clear from these figures that anomalous transport can cause enhanced plasma heating in specific regions. The "hot spot" near the backplate at the cathode root has been observed in our previous study[1] and has been suspected to play a role in backplate erosion. Backplate erosion is the only erosion mechanism that has been shown experimentally[19, 20] to occur along with the appearance of "instabilities" in the terminal voltage of the thruster. It can be noted from Fig. (11) that in the absence of microinstabilities this "hot-spot" disappears. The presence of such a spot has not been established experimentally yet and could provide a check on the predictive ability of the model.

Finally, we show in Fig. (13) (T_i/T_e from the classical run) and Fig. (14) (T_i/T_e from the anomalous run) that microturbulence may be at least partly responsible for the fact that T_i/T_e can exceed unity in the MPD thruster as is well known from experiments. This ratio never exceeded unity in our classical runs.

Conclusions and Final Remarks

A fluid flow simulation model for the self-field MPD thruster has been developed including the effects of plasma wave microinstabilities on momentum and energy transport. Despite the simple constant cross-section geometry adopted, performance predictions from models with microturbulent transport compare more favorably with experiments than do predictions from models without such anomalous effects. Furthermore, the distribution of current, resistivity and heavy species temperature within the thrust chamber shows heat dissipation patterns which may explain some features of MPD thruster operation such as the anode drop and backplate erosion.

There remains a host of improvements that can be applied to the model presented above. These include, coordinate transformation algorithms for simulating more realistic geometries, an accurate representation of viscosity and non-equilibrium rate kinetics and most urgently, in light of the recent measurements in ref. [21] (that confirmed earlier speculations of anomalous ionization) more realistic ionization models including microturbulent effects.

References

[1] G. Caldo, E.Y. Choueiri, A. J. Kelly, and R. G. Jahn. An MPD code with anomalous transport. In 22^{nd} *International Electric Propulsion Conference*, Viareggio, Italy, 1991. IEPC-91-101.

[2] A. Jameson. Transsonic flow calculations. Technical Report MAE 1651, Princeton University, Princeton, New Jersey, 1984.

[3] E.Y. Choueiri, A. J. Kelly, and R. G. Jahn. Current-driven plasma acceleration versus current-driven energy dissipation Part III : Anomalous transport. In 28^{th} *Joint Propulsion Conference*, Nashville, TN, 1992. AIAA-92-3739.

[4] R.G. Jahn. *Physics of Electric Propulsion.* McGraw-Hill, New York, 1966.

[5] S. Miller and M. Martinez-Sanchez. Viscous and diffusive effects in electrothermal and MPD

arcjet thrusters. In 22nd *International Electric Propulsion Conference*, Viareggio, Italia, 1991. IEPC 91-060.

[6] P.C. Sleziona, M. Auwter-Kurtz, and H.O. Schrade. MPD thrusters calculations considering high ionization models. In 22nd *International Electric Propulsion Conference*, Viareggio, Italia, 1991. IEPC 91-087.

[7] H. Maecker. Plasma jets in arcs in a process of self-induced magnetic compression. *Z. Phys.*, 141(1):198–216, 1955.

[8] E.H. Niewood and M. Martinez-Sanchez. A two-dimensional model of an MPD thruster. In 22nd *International Electric Propulsion Conference*, Viareggio, Italia, 1991. AIAA 91-2344.

[9] E.Y. Choueiri. *Electron-Ion Streaming Instabilities of an Electromagnetically Accelerated Plasma.* PhD thesis, Princeton University, Princeton, NJ, USA, 1991.

[10] E.Y. Choueiri, A. J. Kelly, and R. G. Jahn. Current-driven plasma acceleration versus current-driven energy dissipation part II : Electromagnetic wave stability theory and experiments. In 22nd *International Electric Propulsion Conference*, Viareggio, Italy, 1991. IEPC-91-100.

[11] D.L. Tilley. An investigation of microinstabilities in a kW level self-field MPD thruster. Master's thesis, Princeton University, Princeton, NJ, USA, 1991.

[12] D.L. Tilley, E.Y. Choueiri, A.J. Kelly, and R.G. Jahn. An investigation of microinstabilities in a kW level self-field MPD thruster. In 22nd *International Electric Propulsion Conference*, Viareggio, Italy, 1991. IEPC-91-122.

[13] E.Y. Choueiri. A scaling strategy for the preliminary design of MPD thrusters. Master's thesis, Syracuse University, Syracuse, New York, 1983.

[14] M. Mitchner and C.H. Kruger. *Partially ionized Gases.* Wiley Interscience, New York, 1973.

[15] M. Jayaram and A. Jameson. Multigrid solutions for the Navier-Stokes solutions for flow over wings. In 26th *Aerospace Science Meeting*, Reno, Nevada, 1988. AIAA-88-0705.

[16] R.L. Burton, K.E. Clark, and R.G. Jahn. Measured performance of a multi-megawatt MPD thruster. *Journal of Spacecraft and Rockets*, 20(3):299–304, 1983.

[17] J.H. Gilland. The effect of geometrical scale upon MPD thruster behavior. Master's thesis, Princeton University, Princeton, NJ, USA, 1988.

[18] A.D. Gallimore, A. J. Kelly, and R. G. Jahn. Anode power deposition in MPD thrusters. In 22nd *International Electric Propulsion Conference*, Viareggio, Italy, 1991. IEPC-91-125.

[19] D.D. Ho. Erosion studies in an MPD thruster. Master's thesis, Princeton University, Princeton, NJ, USA, 1981.

[20] R. A. Rowe. Ablation of an MPD thruster. Master's thesis, Princeton University, Princeton, NJ, USA, 1981.

[21] T.M. Randolph, W.F. Von Jaskowsky, A. J. Kelly, and R. G. Jahn. Measurement of ionization levels in the interelectrode region of an MPD thruster. In 28th *Joint Propulsion Conference*, Nashville, TN, 1992. AIAA-92-3460.

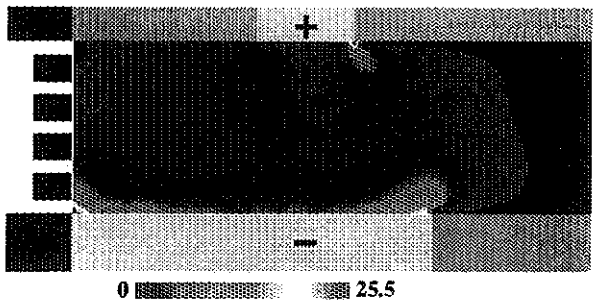

Figure 9: Electron Hall parameter in regions where anomalous transport is active ($u_{de}/v_{ti} \geq 1.5$). Critical regions are those with higher values of the Hall parameter.

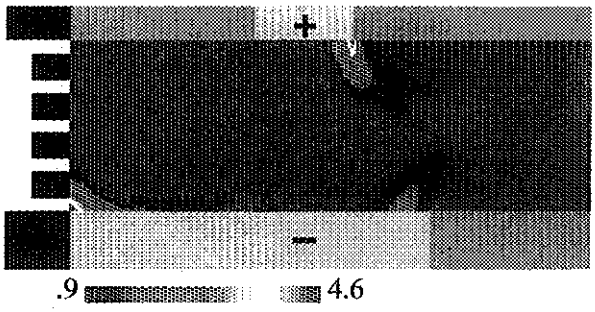

Figure 10: Ratio of "anomalous" to "classical" resistivties (i.e. using the resistivities calculated from the anomalous and classical runs). ($J = 18kA$, $\dot{m} = 6g/s$).

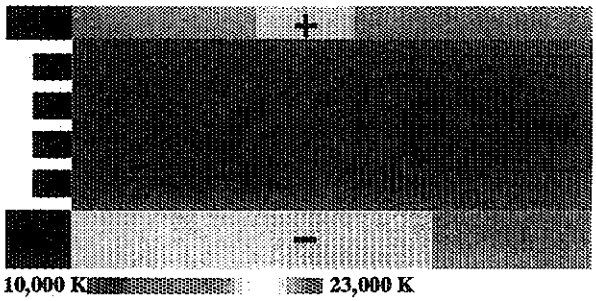

Figure 11: Heavy species temperature for the simulation with classical transport ($J = 18kA$, $\dot{m} = 6g/s$).

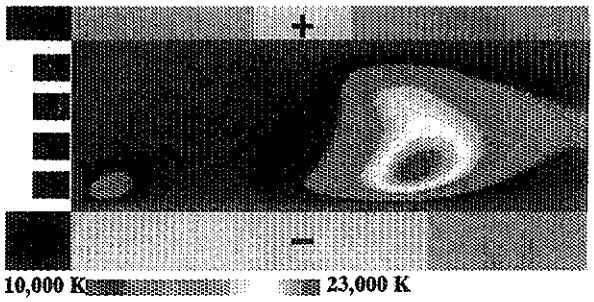

Figure 12: Heavy species temperature for the simulation with anomalous transport showing regions with enhanced ion heating due to microturbulence. ($J = 18kA$, $\dot{m} = 6g/s$).

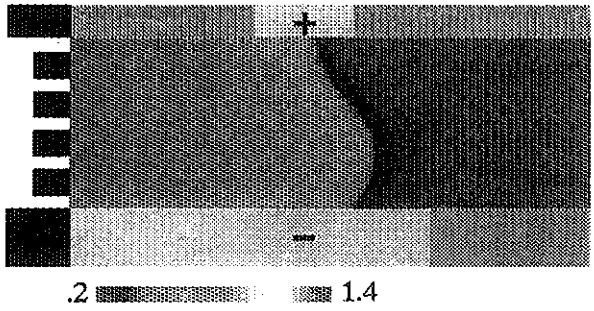

Figure 13: Ratio of ion to electron temperatures for the simulation with classical transport ($J = 18kA$, $\dot{m} = 6g/s$). Note that this ratio nowhere exceeds unity.

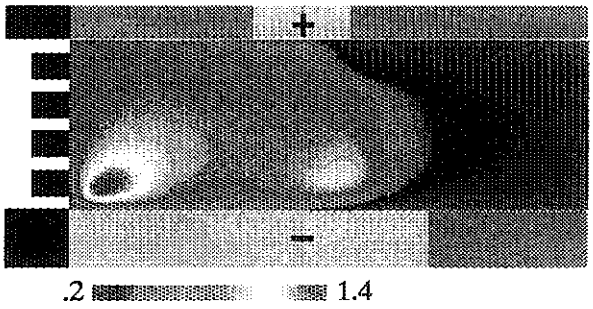

Figure 14: Ratio of ion to electron temperatures for the simulation with anomalous transport ($J = 18kA$, $\dot{m} = 6g/s$).